Unsteady aerodynamics analysis and modelling of a Slingsby Firefly aircraft: Detached-Eddy Simulation model and flight test validation

Neves, A. F., Lawson, N. J., Bennett, C. J., Khanal, B. & Hoff, R. I.

Unsteady Aerodynamics Analysis and Modelling of a Slingsby Firefly Aircraft: Detached-Eddy Simulation Model and Flight Test Validation

Neves, A.F.[a], Lawson, N.J.[a,*] Bennett, C.J.[b], Khanal, B.[c], Hoff, R.I.[a]

[a]National Flying Laboratory Centre, Cranfield University, Cranfield MK43 0AL

[b]Department of Aerospace Engineering, Embry-Riddle Aeronautical University

3700 Willow Creek Road, Prescott, AZ, 86301, U.S.A.

[c] Coventry University, Priory Street, Coventry, United Kingdom, CV1 5FB

Abstract

This paper presents unsteady stall characteristics of a Slingsby T67M260 Firefly light aircraft from both a computational fluid dynamics (CFD) half model and flight tests. Initial results from the steady CFD, based on a RANS $k - \omega$ SST turbulence model, established the critical angle of attack of the stall to be $\alpha_{stall} = 16°$, with a maximum lift coefficient of $C_{Lmax} = 1.2$. Comparisons with straight and level flight test data were comparable up to $\alpha = 12° - 14°$, with the increasing deviation at higher α attributed to the effect of the propeller slipstream under these flight conditions. The RANS CFD model was then extended to an unsteady Detached-Eddy Simulation (DES) model for three angles of attack at pre-stall and stall condition ($\alpha = 14°$, $16°$, $18°$), with analysis of the vortex shedding frequency. Further comparisons were then made with flight test data taken using on-board accelerometers and wing tuft surface flow visualization, at a stalled condition at equivalent α. These unsteady CFD data established a dominant shedding frequency ranging from 11.7 Hz – 8.74 Hz with increasing α and a Strouhal number based on wing chord of St = 0.11, which when compared to flight test accelerometer spectra matched within 2.9% of the measured frequency.

Keywords: Buffet Frequency, Stall, Strouhal Number, Detached-Eddy Simulation, CFD, Flight Test.

*Corresponding author.
E-mail address: n.lawson@cranfield.ac.uk (N.J. Lawson)

1. Introduction

The phenomenon of stall and spin has received continuous attention from the aeronautical industry since the early days of flight [1]. An aircraft spin is an autorotating descent in a helical pattern about the vertical axis [2]. A spin develops when the aircraft is stalled, i.e. the critical angle of attack (α_{stall}) is exceeded, and due to aerodynamics asymmetries or loss of lateral control [3]. The critical angle of attack is the angle after which increasing α will no longer result in an increase in lift. At high α, the adverse pressure gradients on the upper surface of the wing often result in the separation of the boundary layer. If approximately 50% of the boundary layer on the upper surface of the wing is separated, a further increase in the α results in a loss of lift and a significant increase in drag [4]. Usually, before stall occurs a fluid instability develops, buffet, which is a consequence of the separated flow of the wing [5]. Buffet has a characteristic frequency which can be defined through the non-dimensional Strouhal number [6]. The complex separated flow resultant from a stalled aircraft, which is highly three-dimensional and configuration dependent, often results in a design challenge.

The wing of an aircraft is the main component that affects how a stall will develop since it is the main lift generating component and so it determines how the boundary layer separation occurs on the upper surface. The wing section, aspect ratio and taper also dictate the development of the stall and the vortex shedding frequency. Training aircraft, such as the Slingsby T67 require predictable stall characteristics, without a significant rolling moment ('wing drop') at stall. There is also a consideration of the wake development in the stall, due to potential interaction with the aircraft structure, such as the tailplane and fin, as this will both have structural and stability implications for the aircraft.

Furthermore, the design of a spin resistant aircraft requires its stall behaviour to be characterized. Traditionally, this behavior is predicted with theory and data gathered from wind-tunnel testing and flight tests. This may include surface flow visualization with methods such wool tufts and the monitoring of stall related vibrations, i.e., buffet. Ultimately, flight testing is required for certification, but any information early in the design process on stall characteristics will aid the aircraft designer.

Computational Fluid Dynamics (CFD) is now applied as a complementary aircraft design and analysis tool to traditional methods [7]. Although wind-tunnel testing is able to provide data in a greater range of flight envelopes it often fails to meet the flight test conditions. Flight tests are usually performed in a later stage to certify the initial aircraft design and in some cases aerodynamic design fixes are required following initial flight test, which can be costly and difficult to implement. With the maturity of numerical methods, validated CFD is now increasingly being used in the aircraft design process, throughout the aerospace industry [8]. Unsteady CFD methods such as Detached-Eddy Simulation (DES) or Large Eddy Simulation (LES) are also offering the potential to identify complex aerodynamic phenomena, not easily observed during the design or wind tunnel testing. Recent hybrid RANS/LES methods have been

developed to study these unsteady flow phenomena such as boundary layer transition and separation [9].

2. Computational Solver

The commercial CFD solver FLUENT was used to simulate the 3D aircraft geometry considered in this paper. FLUENT is a finite-volume solver and the temporal and spatial discretization schemes available in it provide at most second-order accuracy in space and time. Many studies ([10], [11]) have shown FLUENT to be capable of simulating unsteady flow problems, and of resolving the flow structures around complex 3D geometries when suitably designed computational mesh and time-step sizes are used. Options for both explicit as well as the implicit time-stepping are available with the solver. The implicit time-stepping option was used on the simulated case presented in this research.

For the modelling of the turbulence in the flow, DES based on the $k - \omega$ SST formulation was used. The DES model was chosen in this research to improve the turbulent flow predictions in the regions with significant separated flows. DES is essentially a hybrid LES/RANS model, which uses the standard RANS formulation within the attached boundary layers, and activates a LES Sub-Grid Scale type model in rest of the flow including the separated regions. A typical DES simulation has been known to significantly reduce the computational resource required for the High-Reynolds number wall bounded flows, where using a full-fledged LES modelling would be prohibitively expensive. In the DES formulation, the standard RANS length scale is replaced with a DES length scale defined as follow:

The length scale for the RANS turbulence model $k - \omega$ SST in terms of the turbulence kinetic energy k and the specific dissipation rate ω can be written as,

$$l_{k-\omega} = k^{1/2}/(\beta^* \omega) \tag{1}$$

For the DES formulation, the length scale in the standard RANS equation is replaced by a DES length scale, $\tilde{l}$, which is calculated as:

$$\tilde{l} = min(l_{k-\omega}, C_{DES}\Delta) \tag{2}$$

with $\Delta = max(\Delta x, \Delta y, \Delta z)$ and where C_{DES} is a calibrated constant for the DES model (it is equal to 0.61), and Δ is the largest cell dimension in the local grid. The modified length scale calculated using the relation in Eq. 2 ensures a length scale that is the same as the standard RANS length scale near the walls where $l_{k-\omega} << \Delta$ and reduces to the local grid spacing away from the walls where $l_{k-\omega} << \Delta$. The effect of this is to activate a hybrid turbulence model that behaves as a standard RANS model within the attached boundary layers, and as a LES Sub-Grid Scale model in the rest of the flow including the separated regions.

3. Flight test validation

At the National Flying Laboratory Centre (NFLC) at Cranfield University, flight tests were performed with the Slingsby Firefly T67M260 (see figure 1), a two seat aerobatic training aircraft with a six-cylinder, 260 horsepower normally aspirated engine with fuel injection and inverted lubrication for aerobatic use. Technical specifications can be seen in Table 1.

Figure 1: Cranfield University's Slingsby Firefly T67M260.

Table 1: Slingsby Firefly overall specifications (Adapted from: [12]).

Overall Length	7.55 m
Overall height	2.36 m
Wing Span (b)	10.69 m
Wing Area (S)	12.6 m^2
Dihedral	3° 30'
Incidence at the wing root	3°
Incidence at the Tip	0° 20'
Profile Root	NACA 23 015
Profile Tip	NACA 23 013

3.1. *Straight and Level flight test*

The first flight test was performed at a straight and level condition in which the aircraft was flown at different constant airspeeds, with a maximum speed of 120 knots and the clean configuration stall speed of 62 knots as the minimum. The altitude was constant, in this case 5,000 ft. This flight test was performed in order to determine the lift curve, i.e. the lift coefficient as a function of α, for the pre-stall region.

The direct measure of α during flight was not possible, hence it was estimated using an indirect approach. This consisted of placing a digital inclinometer with a resolution of 0.05°, inside the cockpit on the canopy framework, during the flight test, shown by the red reference line in Figure 2. This canopy line was then referenced to the CFD model canopy and CFD angle of attack as well as the aircraft pitch attitude angle θ during flight.
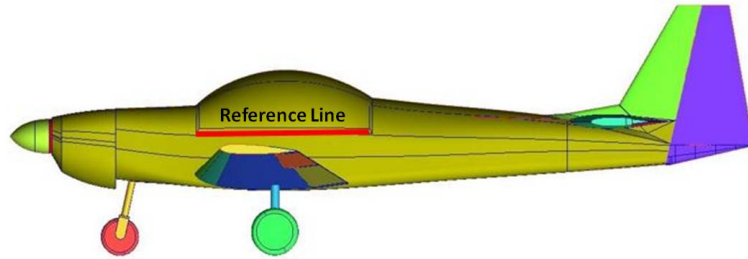
4

Figure 2: Straight and level flight test reference line to estimate α.

The power settings at each indicated airspeed (120, 100, 80, 70, 62 and 60 knots) were then recorded allowing an estimation of aircraft thrust, by equating engine power to the product of the thrust component (equal to drag) and true airspeed (TAS), as outlined in [13]. A pitch attitude was recorded, to equate the horizontal thrust component to drag and a propeller efficiency of 90% was assumed for all cases [14]. The TAS was estimated by taking the indicated airspeed (IAS), corrected to calibrated airspeed (CAS) using aircraft flight manual data and by also recording outside air temperature and the pressure altitude, from the cockpit instruments (see Figure 3) [15]. Engine power was calculated from interpolated aircraft flight manual data, given TAS, altitude corrected to ISA, manifold pressure and tachometer readings (see Figure 3).

Figure 3: Slingsby Firefly instrument panel.

Lift was determined with the aircraft weight given as the sum of pilot, observer, fuel and aircraft empty weight. Here the fuel weight was estimated from a full tank condition at engine start-up and the fuel gauge condition as the time of the measurements. Aircraft empty weight was taken from the flight manual and passenger weights recorded at the time of flight. The lift coefficient C_L was determined based on the lift force divided by the dynamic pressure and wing's area. The lift curve slope and drag polar

were then determined as outlined in reference [13].

The errors for the different variables are listed in Table 2. In a number of cases, the errors are estimated from the resolution of the cockpit gauges or in the case of the CAS data and engine data, from the data presented in the aircraft flight manual (AFM). Where appropriate errors are combined using standard statistical methods [16].

3.2. Stall α Flight Test

The α_{stall} was obtained with two additional flight tests which involved taking the aircraft to a post-stall condition, with GPS derived data, cross-checked with pressure based data where possible. In these additional tests, the aircraft was stalled at a constant deceleration rate and engine idle. In a given sequence, the aircraft was initially maintained in straight and level flight, then increasing α past the stall warner, until the aircraft could not maintain level flight, followed by further increases in α to induce light buffet and eventually heavy buffet, with a significant rate of descent, before initiating stall recovery. In these flights, cross-wind headings and repeats were flown by the pilot, based on current meteorological forecasts for the same altitude band, which enabled the effect of wind component on ground speed to be minimized. No wind estimators were available on the GPS systems.

In the first test, 1Hz GPS altitude and ground speed data was logged using the Runway HD app by Airbox Aerospace Ltd on an iPad Mini 2. In these flights, two cockpit cameras also logged the altimeter and a digital level, mounted on the canopy reference line. From this GPS and inclinometer data, pitch attitude (θ) and flight path angle (λ) was recorded and the sum of θ and λ was used to estimate α. Here λ is calculated using the aircraft forward and vertical speed components where the vertical component is calculated from the GPS derived altitude and rate of descent. In this case, GPS data is assumed to be independent of pressure altitude and θ, thus avoiding pressure errors in any airspeed estimation, when flying cross-wind. As a gross error check, however, altimeter data was also used to cross-check the GPS altitude, up to the point of buffet. At or beyond buffet, pressure errors will be significant and GPS altitude is expected to be more reliable.

In the second stall test, a Pixhawk4 attitude heading and reference system (AHRS), with sample rates of 250 Hz in pitch, roll, yaw and acceleration and 5 Hz in GPS, was used to improve data rate and allow the integration of pitch attitude data into the α estimate. The pitch attitude data was resampled to the GPS data rate of 5 Hz and the same α calculation completed using GPS altitude to estimate λ, but now also using the Pixhawk4 pitch attitude in place of the inclinometer, to finally estimate α. In this case, as before, the assumption is made that the GPS velocity and altitude is independent of pitch attitude and pressure altitude.

These sets of iPad and Pixhawk4 results are shown in Figure 4, with two Pixhawk4 sequences and show the range of stall to be between $\alpha = 13°$ when the cockpit stall warning first activated, up to around $\alpha =$

6

30° when the aircraft was in heavy buffet, which would subsequently lead to a wing drop with a g-break, followed by an autorotation, before the stall recovery by the pilot. Between 7s – 19s in both Pixhawk4 sequences, although the aircraft was stalled and descending with an flight path angle of around $= 5°$, and α are only slightly varying as the pilot gradually increases the elevator up position, up to the point where buffet was first observed. Variations in and α at this point, are in part attributed to the repeatability of the elevator input and in one sequence show reducing for a period. This gradual development of a stall is characteristic of trailing edge stall, expected for this type of airfoil section [17] and is also evidenced in the CFD lift-curve slope shown in the subsequent sections of this paper. As the heavy buffet developed, the aircraft was then seen to pitch up and down significantly as the moments providing longitudinal stability became increasingly unbalanced, which is a characteristic of high α behavior, where stability is reduced [18]. These pitch excursions are evident in the Pixhawk4 and movie data in the region of heavy buffet and predicates a developing incipient spin, which follows a wing drop. The significant excursions in the Pixhawk4 data also corresponded well to the altimeter behavior seen in the movie and the altitude at which the aircraft was subsequently recovered to level flight. These results were subsequently used to set the α range for the computational model, where it is estimated that the stall and C_{Lmax} is occurring at $\alpha = 15°$ - 20°, with increasing buffet, then with heavy buffet experienced above 20°.

Errors for the λ and α from these stall flights are summarized in Table 3. In the Pixhawk4 unit, a Q-attitude estimator was enabled for all inertial data, which is a quaternion based complementary filter for attitude, as outlined in the Pixhawk4 v1.9 manual. The 5Hz GPS Pixhawk4 data is unfiltered and is the main source of noise in the λ and α calculation, where a simple two-point moving average has been used, so to retain the transient excursions post-buffet. Future work is planned to improve the filtering of this data. For the iPad, at the time of writing, no information was available from Apple to assess the GPS and inertial filtering, although when compared to the Pixhawk4 data, it is likely the iPad GPS data is filtered, given the lower levels of uncertainty in Table 3.
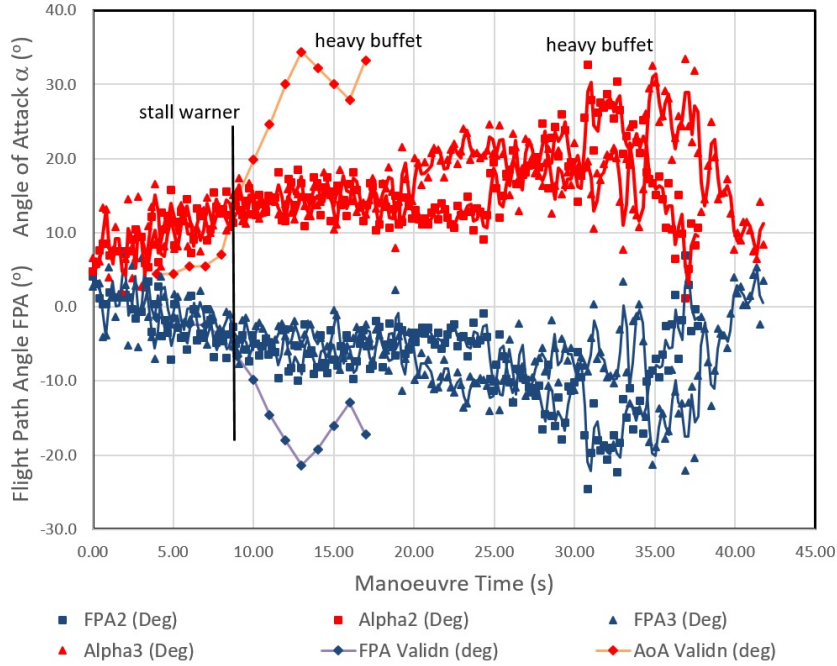
Figure 4: Flight path angle and as a function of flight time (N.B. Validation data from digital level test is included for comparison – FPA Validn, AoA Validn).

Table 2: Errors from variables derived from cockpit instruments and AFM (AFM – aircraft flight manual, % FS – percent of full scale measurement, FS – full scale).

Variable	Error	Source	Comments
outside air temperature (°C)	±5	gauge	cockpit instrument
altitude (ft)	±10	gauge	cockpit instrument
indicated airspeed (knots)	±2.5	gauge	cockpit instrument
calibrated airspeed (knots)	±1	AFM	AFM airspeed correction data for zero flap
true airspeed (% FS)	±3.4	calculated	conversion from [15] including airspeed, altitude and temperature errors (FS – 129 knots)
fuel quantity (kg)	±10	gauge	cockpit instrument
aircraft empty mass (kg)	±20	AFM	estimated from weighing schedule
manifold pressure (inHg)	±1	gauge	cockpit instrument
engine speed (rpm)	±50	gauge	cockpit instrument
power (%)	±2	AFM	performance tables
thrust (% FS)	±3.9	calculated	use variables power, true airspeed and pitch attitude, assume propeller 90% efficient [14] (FS – 2280N)
lift (% FS)	±3.1	calculated	use total weight (FS – 9640 N)
lift coefficient (C_L)	±4.9	calculated	including weight, calculated density and true airspeed errors (FS – 1.13)
drag coefficient (C_D)	±5.4	calculated	including thrust, calculated density and true airspeed errors (FS – 0.199)
pitch attitude (°)	±2.5	attitude indicator	cockpit instrument - gross error check for λ

8

Table 3: Errors from variables derived from GPS and digital level instruments (CI – confidence interval, FS – full scale).

Variable	Error	Source	Comments
digital level α (°)	±2	digital level	estimated error from observation of pre-stall in-flight movie of instrument in level flight
iPad λ error (°)	±2.6	calculated	95% CI assessed from sample in stable flight
iPad α error (°)	±2.6	calculated	95% CI assessed from sample in stable flight
Pixhawk4 velocity error (m/s)	±0.1	Pixhawk NEO-M8 GNSS chipset datasheet	95% CI from sample data sheet
Pixhawk4 altitude error (m)	±7.5	Pixhawk NEO-M8 GNSS chipset datasheet	95% CI assuming 4 satellite fix and autonomous lateral position from data sheet
Pixhawk4 attitude error (°)	±0.2	Pixhawk ICM-20689 IN chipset datasheet	based on maximum noise spectral density with FS 250 °/s at 250Hz
Pixhawk4 λ error (°)	±4.1	calculated	95% CI assessed from sample in stable flight
Pixhawk4 α error (°)	±4.1	calculated	95% CI assessed from sample in stable flight

3.3. *Flow visualisation flight test with wool tufts*

In order to be able to identify the boundary layer flow separation patterns on the upper surface of the wing, flow visualisation techniques in-flight were required. The most suitable flow visualisation techniques to observe flow direction and boundary layer separation are either flow cones and tufts, or emitted fluid technique. The wool tufts visualisation technique, presented here, was based on work published by Hoff and Gratton [12].

The flight test recorded the boundary layer separation during the stall, by observing the wool tufts using an HD camera up to the point where the wing dropped. The aircraft was stalled twice by reducing its speed to the stall speed of 62 knots ($\approx$ 32 m/s), using engine idle, maintaining level flight and in a clean cruise configuration. The wool tufts were placed on the boundary layer (estimated to be up to $\delta = 2.4\ cm$).

To perform the test, the left wing of the Slingsby Firefly was covered by wool tufts of 5 mm thickness 15 cm length in a structured pattern, i.e., the tufts were vertically and horizontally spaced 24 cm. This arrangement was based on the work developed by Hoff and Gratton [12].

Due to the fuel tank and taper of the wing some of the tufts were reduced in length and spacing in order to be able to cover most of the wing upper surface. The tufts schematic is shown in Figure 5, where the green arrows represent the spacing and the blue arrows the length of the wool tuft. This resulted in

62 wool tufts that were attached to the upper surface of the wing with masking tape. An Akaso EK7000 HD camera, with a frame rate of 25 Hz, was then mounted inside the cockpit using a Gecko sucker mount, providing a view towards the wing in order to record the wool tufts behaviour during the flight.

Figure 5: Wool tufts scheme on the upper surface of the wing.

3.4. *Buffet Flight Test*

Before the in-flight stall buffet measurements, a ground test was conducted to obtain the natural frequency of the wing, to ensure sufficient discrimination between the structural and aerodynamic buffet frequencies. Accelerometers were mounted on the tip of the wing and a mechanical impulse was given on the wing. In Figure 6, it is observed that the natural frequency of the wing is 6.3 Hz.
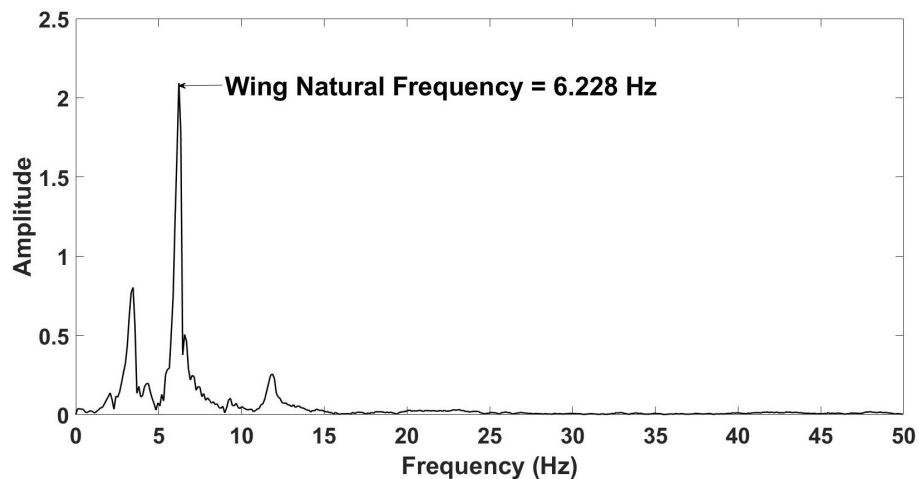

Figure 6: Natural frequency of the wing.

For the flight test, in order to identify the buffet frequency, the Slingsby's cockpit was equipped with three accelerometers (Shimmer3 IMU Units), as shown in Figure 7 and data recorded from a series of stalls. The data frequency acquisition was 100 Hz and a Fast Fourier Transform analysis (FFT) was

performed in order to convert the signal in the time domain to the frequency domain.

Figure 7: Position of the three accelerometers inside the aircraft's cockpit.

In this flight test there was also a second HD camera with a cockpit view, in order to synchronize the sensors with the events. In order to monitor the accelerometer measurements with the cockpit camera, each sensor was visibly tapped while approaching the stall. The signal can be seen as an initial peak in the sample captured by one of the accelerometers, shown in Figure 8. Both cameras were then subsequently synchronised using the stall warning sound in the cockpit. From the same sample, it is observed that the buffet had a duration of four seconds and that there is a g-break representing the initial development of an incipient spin, as discussed previously.
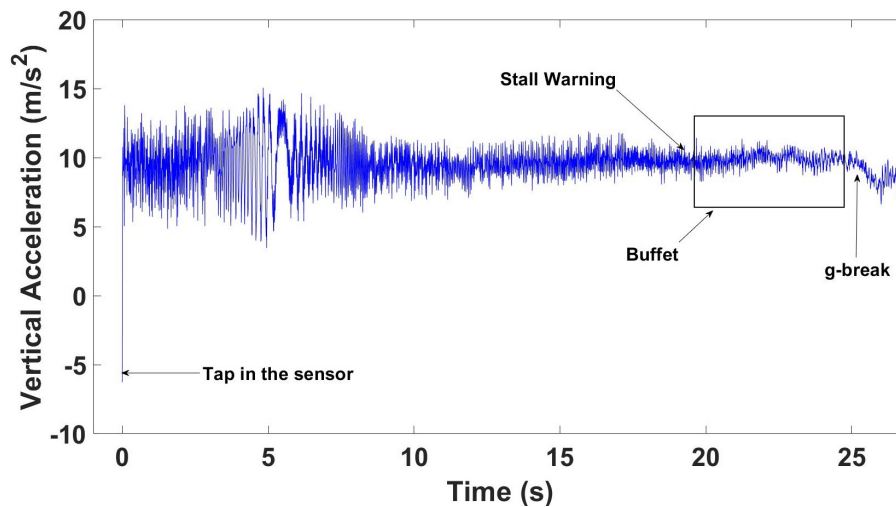

Figure 8: Data signal from one the accelerometers obtained from the buffet flight test.

4. CFD Methodology

4.1. *Mesh Parameters*

A half model of a Slingsby Firefly model was meshed using ANSYS ICEM CFD. The first step was to generate a computational fluid domain. The fluid domain adopted for the flow calculations was a semi-cylinder described in a Cartesian coordinate system (x, y, z). Due to the boundary conditions applied, the domain must be large enough so that the boundary conditions can be met. Hence, it is advised that

the domain size is set to be 10 times the largest characteristic length of the body being studied. The largest characteristic length is the fuselage length (L). The domain possesses an inlet, outlet, far field and symmetry plane. Thus, the inlet distances were set as 10L from the aircraft, the outlet 15L and the radius of the cylinder is 5L.

A hybrid mesh was generated intially with a top-down approach Octree method with prism layers representing the boundary layer. The final mesh was computed with the Delaunay method, a bottom-up approach which requires an initial surface mesh, which was set as triangular in this case with prisms and tetrahedra for the fluid volume. The hybrid mesh generated for the aircraft model is shown in Figure 9.
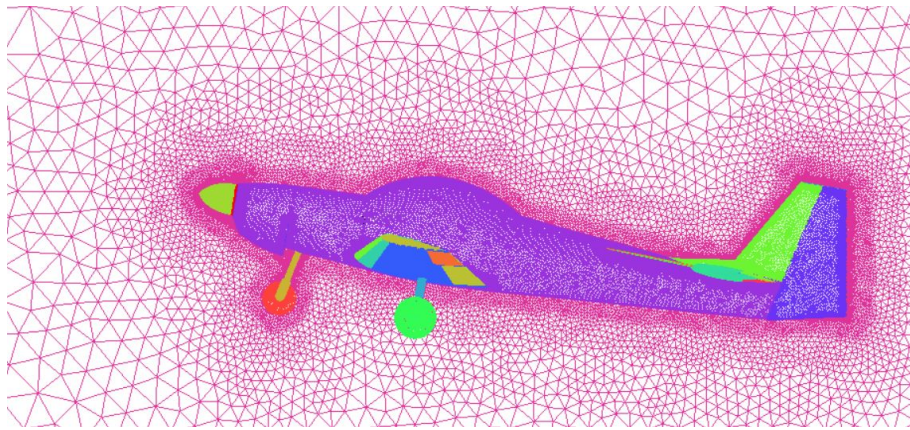

Figure 9: CFD hybrid mesh of the Slingsby Firefly.

An unstructured mesh allows for a rapid local mesh refinement for both RANS and DES flow calculations, permitting complex geometries and also allowing for the generation of a density region. According to Spalart [19], there are several mesh regions required with different densities. In this particular work, the region of interest is the wing's wake where the vortex shedding is computed. This is the focus region where nearly isotropic cells are required in order to resolve unsteady and time-dependent features. Hence, a density region with near isotropic cells is generated with a region of around 0.8L, with a grid spacing (Δ) of 0.03 m, which is 2.5% of the mean aerodynamic chord. The focus region is shown in Figure 10.
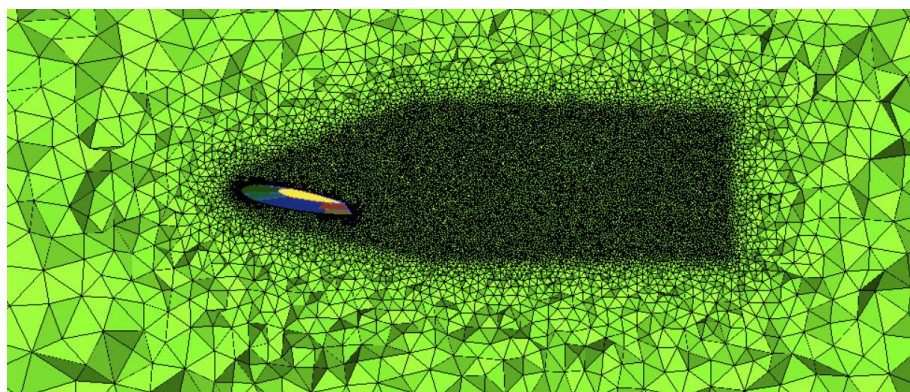

Figure 10: Mesh density region representing DES focus region.

In order to model the boundary layer in the mesh, prism layers were created. The thickness of the prism boundary layer (δ) was estimated by assuming a turbulent boundary from:

$$\delta \approx \frac{0.37\bar{c}}{Re^{\frac{1}{5}}} \, . \tag{3}$$

Where $\bar{c}$ is the mean aerodynamic chord of the wing and the Reynolds number (Re) is based on the mean aerodynamic chord ($\bar{c}$), and is computed as:

$$Re = \frac{\rho V \bar{c}}{\mu} \, . \tag{4}$$

where ρ is the density, V is the velocity and μ the dynamic viscosity.

The simulations were performed with a flow speed of 31.9 m/s, which is 62 knots representing the stall speed of the aircraft in a clean configuration, i.e., with a bank angle of 0°. The flow properties used were based on ISA at a density altitude of 5000 ft.

For the prism layers an initial height and total height were set so that the three regions of the turbulent boundary layer, viscous layer, buffer layer and log-law region were modelled [20]. Hence, a dimensionless wall distance of $y^+ < 1$ and of $y^+ = 1000$ were used to ensure the outer layer is captured. The first cell height is obtained using the following expression:

$$y^+ = \frac{\rho U_\tau y}{\mu} \, . \tag{5}$$

with a chord Reynolds number of $2.3 \cdot 10^6$. Obtaining the friction velocity (U_τ) is accomplished by computing the skin friction coefficient (C_f), followed by the wall shear stress (τ_w) and finally calculating the friction velocity. This process is accomplished with equations 6, 7 and 8 such that:

$$C_f = 0.058 \cdot Re_l^{-0.2} \, . \tag{6}$$

$$\tau_w = \frac{1}{2} \cdot C_f \cdot \rho \cdot U_\infty^2 \, . \tag{7}$$

$$U_\tau = \sqrt{\frac{\tau_w}{\rho}} \, . \tag{8}$$

leading to an initial cell height of $y^+ = 9 \cdot 10^{-6}$ m and a final cell height of 0.0047m, using an expansion ratio of 1.2 and 22 prism layers, also given $\delta = 0.024$m. The summary of the boundary layer parameters computed are shown in Table 4.

Table 4: Mesh boundary layer parameters.

Re	δ	$\delta^+ = 0.2$	C_f	τ_w	u_τ	Δ_{y_1}	N
$2.3 \cdot 10^6$	0.024	0.0047	0.0031	1.664	1.256	$9 \cdot 10^{-6}$	22

4.2. Numerical Solving and Boundary Conditions

The flow calculations were performed with ANSYS Fluent. The density-based solver was applied and the DES flow calculations were initiated after RANS converged solutions were obtained. The convergence was obtained by assuring a decrease in globally scaled residuals of less than 10^{-3} and when the monitored lift and drag coefficients oscillated with scaled values of less than 10^{-4} of RMS. The density of the air inside the fluid volume was treated as an ideal gas and the viscosity described by the Sutherland law [21] . The CFD model possesses five boundaries: inlet, outlet, far field, symmetry plane and the aircraft model. The flow vector was set as $(1, 0, 0)$, i.e., in the positive x direction, as the model was set at an angle of α to this axes. The boundary conditions applied were based on several studies performed on an aircraft [20], [22], [21], [23]. At the inlet, outlet and far field, pressure far field boundary conditions were applied. At the symmetry plane located at $z = 0$, symmetry conditions were applied. At the aircraft surface due to the no-slip and impermeability, the wall boundary condition was applied.

The unsteady calculations were performed with DES $k - \omega$ SST after the converged steady RANS solutions were obtained. The previously mentioned settings remained the same, however the time step of 0.00067 s was defined following the DES guidelines of Spalart [24]. Spalart states that the time step is computed as the division between the grid spacing (Δ) of the focus region and the highest velocity found in the same region. The maximum speed found is usually 1.5 times more than the free stream velocity, hence the time step was computed with a velocity of 45 m/s.

RANS flow calculations were performed to eight different α's: $5, 10°, 12°, 14°, 16°, 18°, 20°$ and the DES flow calculations were only performed to the α where buffet was observed 14,16 & 18 °.

A mesh sensitivity analysis was performed in order to evaluate the most suitable mesh density that the simulations could be performed. Three different mesh densities were used to perform the mesh sensitivity analysis, at a pre-stall $\alpha = 12°$ and a post-stall $\alpha = 18°$. The coarse mesh had a total of 7.57, the medium had 11.3 and the fine mesh had 17.15 million cells.

The mesh sensitivity analysis for an $\alpha = 12°$ is shown in Table 5. The medium density mesh presented the best balance between the deviation observed compared to the fine mesh and the computational time. Hence, all the CFD flow calculations were performed with the medium density mesh.

Table 5: Mesh sensitivity analysis: Lift and Drag coefficients and respective relative deviations for the flow calculations at α=12 °.

N° of cells	C_D	ΔC_D (%)	C_L	ΔC_L (%)	T(h)
7.57	0.131	5.645	1.074	-6.771	31
11.3	0.127	2.419	1.129	-1.997	59
17.15	0.124	-	1.152	-	85

5. Results

5.1. *Lift curve*

Figure 11 shows the results of the straight and level flight test performed in the Slingsby Firefly. The lift curve obtained from the flight tests shows a linear behaviour indicating that the α reached are in the pre-stall region. The best fit curve for the lift slope is $C_L = 0.0939\alpha + 0.0674$, with α in degrees. The results for each indicated airspeed tested are shown in Table 6.
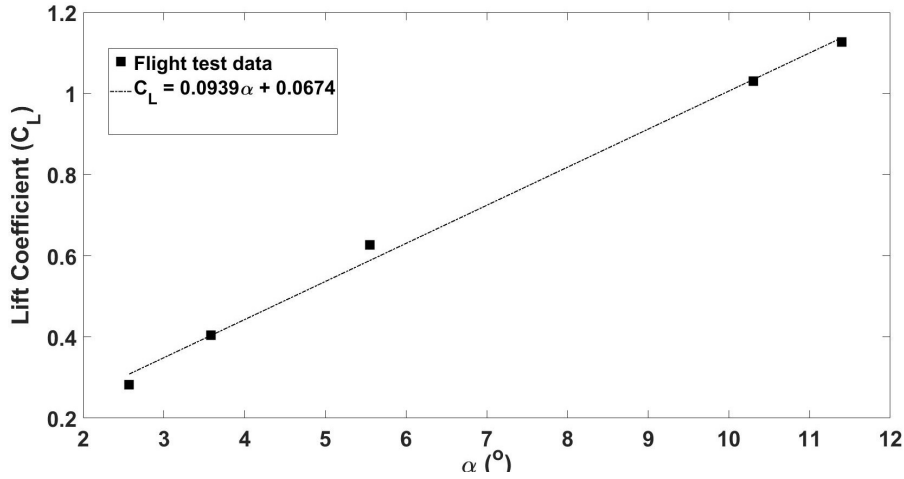

Figure 11: Lift coefficient as a function of the α obtained from the straight and level flight test.

Table 6: Flight test results: α and respective lift coefficient.

IAS (knots)	α (°)	C_L	C_D	L/D
120	2.57	0.282	0.067	4.235
100	3.58	0.405	0.0973	4.161
80	5.55	0.627	0.174	3.595
70	9.69	0.809	0.191	4.248
62	10.3	1.031	0.2314	4.453
60	11.4	1.127	-	-

The comparison between the CFD and flight test lift coefficient is shown in Figure 12. The lift curve obtained from the steady RANS calculations has two distinct regions: a region where a linear behaviour is observed up until a certain angle is reached, i.e., α_{stall} that corresponds to the maximum lift coefficient, and a region after which the increase of angle of attack no longer produces more lift.

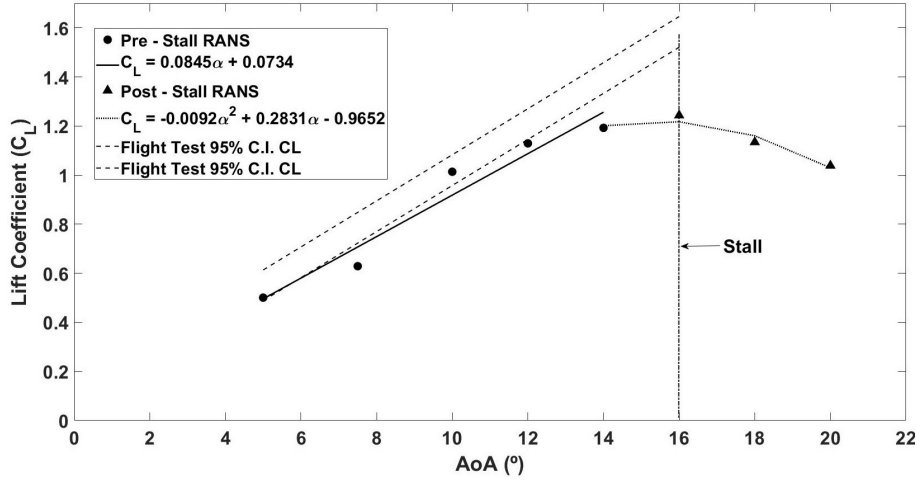The first region of the CFD results ($\alpha = $ 5-14°) corresponds to an approximately linear variation of

Figure 12: CFD and flight test comparison of lift curves obtained.

lift, this means an increase in α would result in a direct increase in lift. The linear curve is defined by : $C_L = 0.0845\alpha + 0.0734$. For the CFD results, the values of α_{stall} and C_{Lmax} are 16° and 1.244, respectively.

The second region of the curve corresponds to the post-stall conditions with significant separation. In this case, from the C_{Lmax} up to $\alpha = 20$ ° there is a decrease of 0.206 in the value of the lift coefficient, indicating trailing edge stall and a gradual loss of lift, consistent with this type of aerofoil section and Re. This result in C_{Lmax} and α is also consistent with the results from the flight test.

With reference to Figure 12, the steady RANS solutions have a lift curve slope that differs 10% from the lift slope obtained from the flight tests and the zero lift angle is 20% lower for the CFD calculations. This results in a general under prediction of the lift coefficient obtained from the CFD flow calculations.

A contribution for this under prediction is the lack of propeller thrust in the CFD model since the flight tests were powered. The propeller augments lift over the section of the wing, affected by the propeller slipstream [22]. The slipstream over the wing encourages flow attachment up to a higher α, thus different α_{stall} between the flight tests and the CFD data should be expected.

5.2. *Surface Flow Visualisation*

The CFD surface visualisation streamlines for the α studied are shown in Figure 13. The Slingsby Firefly has a tapered wing with geometric washout, i.e., the angle of incidence at the root is higher than at the tip. As the angle of attack is increased the flow begins to separate at the root due to its washout. Further increase of the α will result in an increase of flow separation in both span-wise and chord-wise directions. The aerofoils used in the wing are both thick aerofoils hence a trailing-edge stall is present. This progression of flow separation is shown in Figure 13.

The aircraft will stall when about 50% of the wing's upper surface flow is separated resulting in a loss
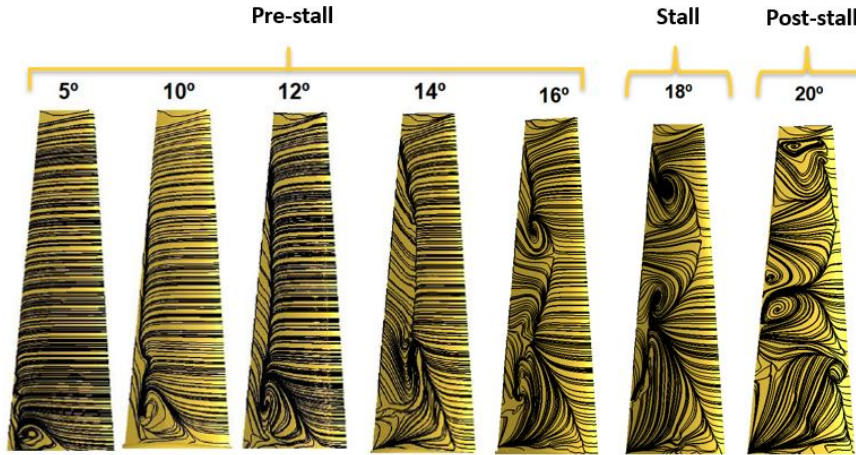
Figure 13: Streamlines contours of the different α studied with RANS k-ω SST.

of lift. The $\alpha = 16°$ limiting streamline contour shows that about 50% of the flow is separated and the respective flow separation area was calculated in order to confirm this. The results are shown in Table 7 and the respective schematic is shown in Figure 14. The percentage of the total area correspondent to the boundary layer flow separation was 49 %, which means that the aircraft is stalled at this α.
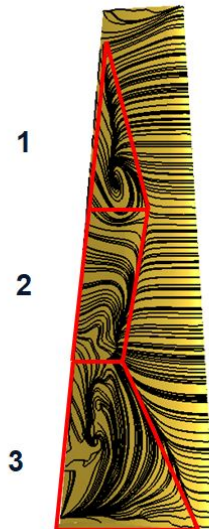

Figure 14: Flow separation area schematics represented in Table 7.

Table 7: Percentage of the boundary flow separation of the upper surface of the wing for an α= 16°.

Region	Area (m^2)	Flow separation (%)
Upper Surface	5.543	-
1	0.455	8.208
2	0.659	11.889
3	1.582	28.541
Total flow separation		48.638

17

The results were compared with images from wool tufts visualisation in-flight. The boundary layer flow separation patterns and progression is similar to the one encountered in the CFD flow visualisation, both in terms of the separation pattern and size. These comparisons are shown in Figure 15 for a range of α, where key separation lines have been annotated onto the camera images. More complex surface flow patterns are also present on the CFD, with similar evidence on the camera images, including the presence of a "mushroom" convergence structure seen at 18 degrees. This flow feature will be discussed in a future paper and has been reported in wind tunnel tests by Katz and Weiss [25].
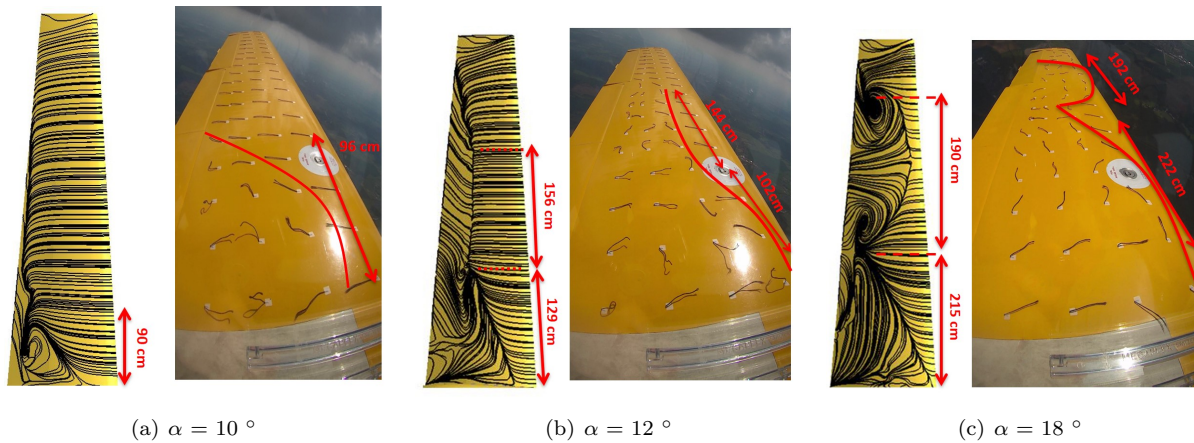

(a) $\alpha = 10\,^{\circ}$ (b) $\alpha = 12\,^{\circ}$ (c) $\alpha = 18\,^{\circ}$

Figure 15: CFD and flight test flow visualization of the boundary layer on the upper surface of the wing.

5.3. Buffet Frequency

The DES model was implemented after a converged RANS solution of the $\alpha = 14°$, $16°$ and $18\,°$ was obtained to examine the buffet frequency. The frequency of the shed vortices (f_s) was computed at four probes located at different regions in the wake of the wing shown in Figure 16. In addition, the lift coefficient was monitored. A Fast Fourier Transform (FFT) was performed to examine the spectra and the DC component of the signals. Prior to the FFT processing, the MATLAB tool: *detrend* was used. Moreover, the amplitude was normalized for consistency and comparison with the flight test spectra. The results obtained from the CFD calculations were then compared with the buffet frequency of the aircraft when approaching stall.
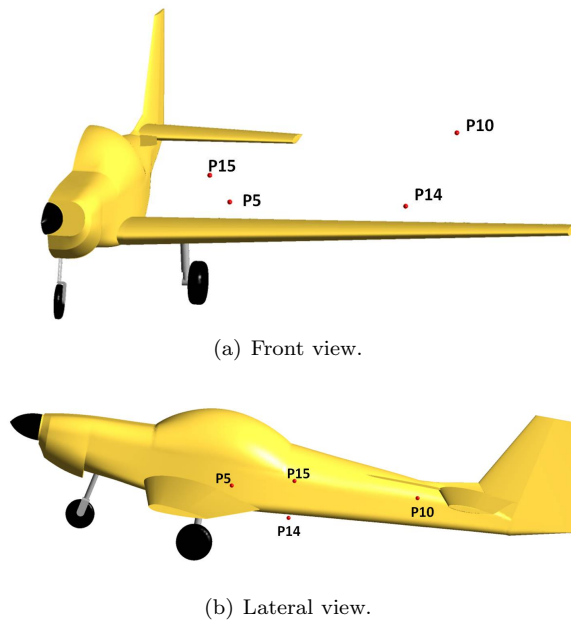
(a) Front view.

(b) Lateral view.

Figure 16: Different views of the static pressure probes in the wing wake.

The FFT was applied to the static pressure for the probes monitored and to the lift coefficient of the three α studied. The time step used was 0.00067s which corresponds to a frequency of acquisition of 1472 Hz. Figure 17 shows the FFT resultant from the data monitored at point P5 of the static pressure. It is observed that in all of the graphs a dominant peak exists which corresponds to the vortex shedding frequency. It should also be noted that the frequency is reducing with increasing α, which is consistent with an increasing separation bubble size, growing from the trailing edge with a fixed chord length. This effect is the subject of a further paper and has also been reported in a previous paper of a DNS study of a NACA 0012 aerofoil [26].
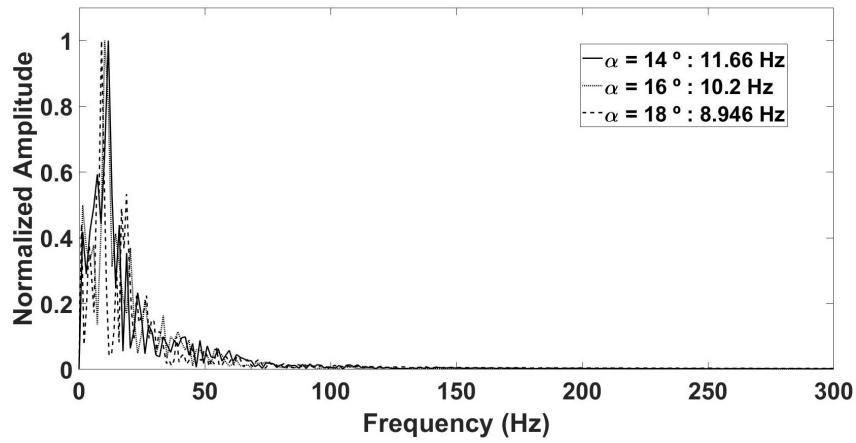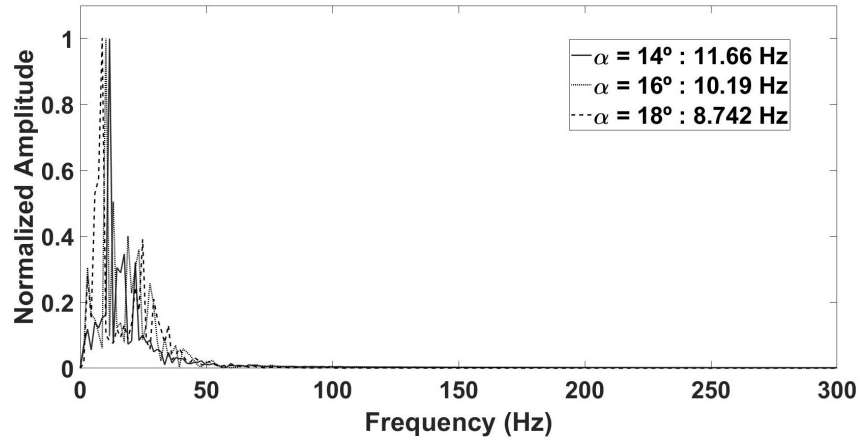
(a) FFT window 300 Hz.
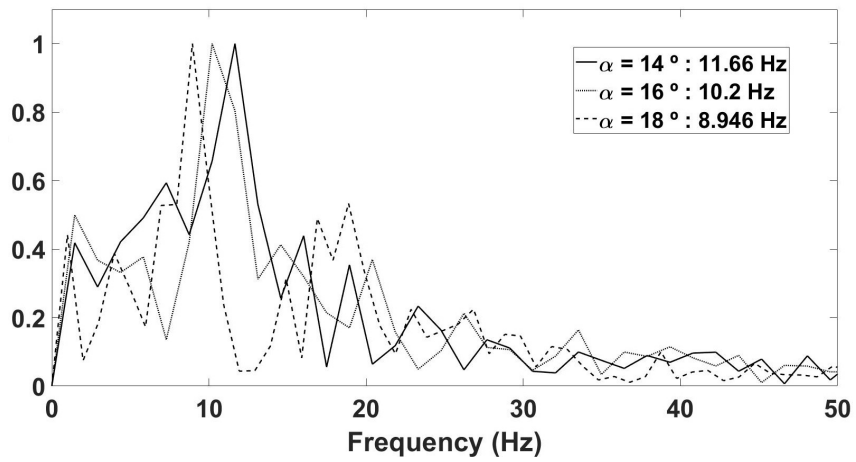
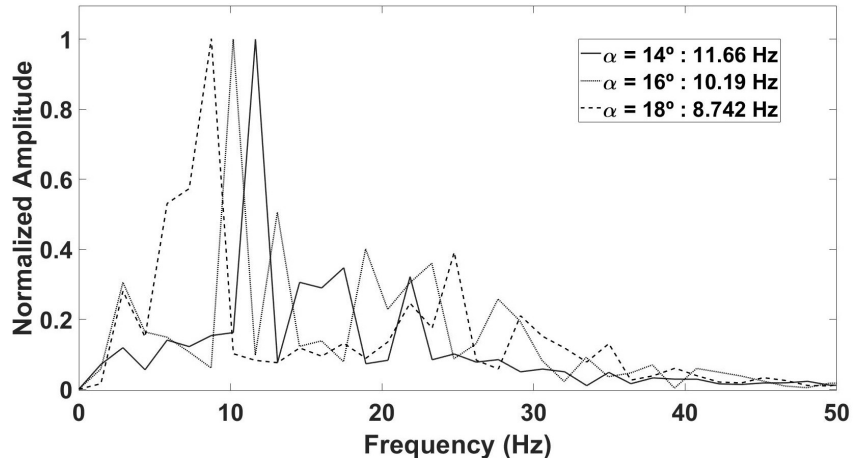(b) FFT window 50 Hz.

Figure 17: Fast Fourier Analysis of static pressure at probe point p5 (sample rate 1472 Hz).

The lift coefficient was also monitored for the α studied and the gathered data is shown in Figure 18. The same trend was found with the increase of the α , i.e., an increase in the α resulted in a decrease in the frequency. These results are summarized in Table 8.

(a) FFT window 300 Hz.

(b) FFT window 50 Hz.

Figure 18: Fast Fourier Analysis of CL for an α=14°, 16° and 18° (sample rate 1472 Hz).

Table 8: Summary of the f_{vs} (Hz) of the probes: P_5, P_{10}, P_{14}, P_{15} and C_L for the $\alpha = 14, 16, 18$ °.

α (°)	$f_{vs}P_5$	$f_{vs}P_{10}$	$f_{vs}P_{14}$	$f_{vs}P_{15}$	$f_{vs}C_L$
14	11.660	11.660	11.660	11.660	11.740
16	10.20	10.20	10.20	10.20	10.190
18	8.946	8.742	8.946	8.946	8.742

In order to validate the quality of the previous CFD results, the buffet frequency was measured in flight. Four seconds of flight data spectra were analysed, the acquisition frequency was 100 Hz, in this case, and the spectra amplitude was normalized.

A detailed analysis was performed to the data from sensor $n°3$, in order to verify if the increase in angle of attack would result in a decrease in the buffet frequency, as observed with the CFD flow calculations. This analysis is shown in Figure 19. From the start of buffet there is an increase of the α as it was observed in the stall α flight test and a correspondent decrease in the buffet frequency. The different peaks in the FFT are due to the signal noise from several vibration sources of the aircraft as

illustrated in Figure 19.

Figure 20 shows the direct comparison of the static pressure data at point P5 at an $\alpha = 14°$ and the first second of buffet recorded during the flight test.
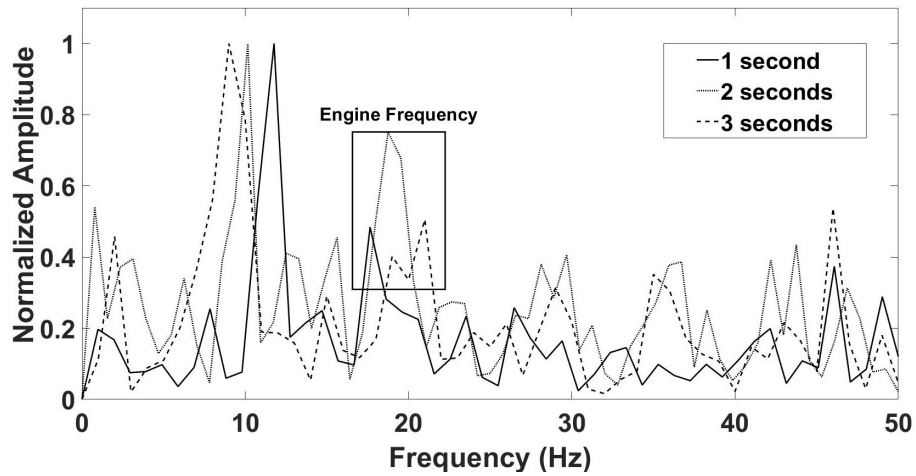

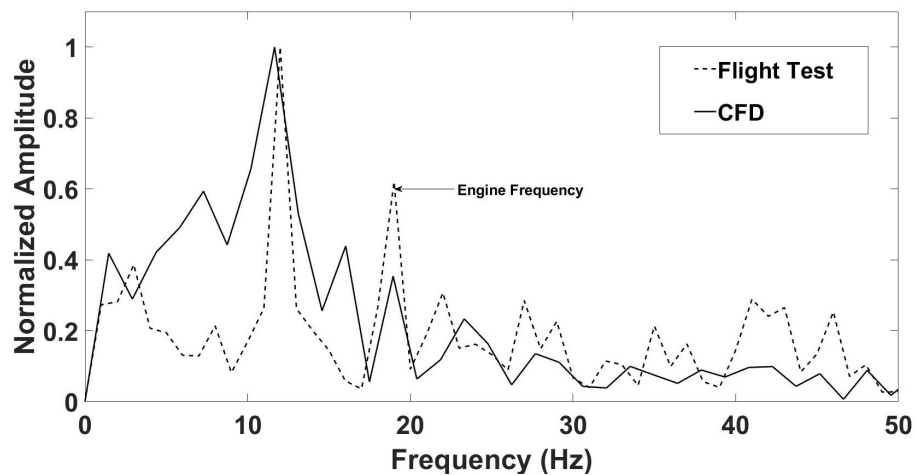Figure 19: FFT analysis of three buffet windows from start of buffet (see Figure 8).

Figure 20: Vortex shedding frequency comparison between CFD and flight tests data.

In Table 9, comparable CFD and flight test results for the frequency of the vortex shedding and buffet, respectively, and its relative deviation are presented. In addition, the Strouhal number (St), based on the projected height, $h = \bar{c} \cdot sin(\alpha)$, was computed for the CFD and flight test results. The values of St varied from 0.1-0.115, which is typical for unswept wings with flow separation (S=0.1-0.2) according to Katz and Plotkin [6], see Table 10.

6. Conclusions

This work has investigated stall characteristics of a Slingsby light aircraft for the pre and post-stall conditions by comparing flight test data to a RANS and DES CFD model, using a k-ω SST turbulence model, up to an angle of attack $\alpha = 20°$.

22

Table 9: Percentage of the relative error of the quantities frequency: P_{static}, and C_L.

α (°)	f_{Flight} (Hz)	$|\Delta_{rel}|_{P_{static}}(\%)$	$|\Delta_{rel}|_{C_L}(\%)$
14	12.0	2.833	2.167
16	10.16	0.394	0.295
18	9.0	0.60	2.311

Table 10: Strouhal Number comparison between flight tests and CFD.

$\alpha(°)$	$St_{Flight\ test}$	$St_{P_{static}}$	St_{C_L}
14	0.115	0.111	0.106
16	0.111	0.105	0.105
18	0.110	0.103	0.10

Results have shown the flight test data generally matches the steady state computation model within experimental error up to $\alpha = 14°$ pre-stall, with the flight test data subsequently diverging at higher alpha. This divergence was thought to be related to the slipstream effect of the propeller, which was not included in the CFD model. Further validation of the boundary separation characteristics up to $\alpha = 18°$, using surface flow visualization from the flight test, also showed a close match to the CFD model, with flow separation growing from the trailing edge. The CFD data also indicated a 'mushroom' type surface flow pattern at the highest α, as reported by previously published work in a wind tunnel, with a similar geometry. At stall the CFD predicts a C_{Lmax} of 1.25 at a stall angle of $\alpha = 16°$, with flight test data indicating a similar condition between $\alpha = 15° - 20°$.

Post-stall both the unsteady CFD and flight test data showed the development of buffet, generated by boundary layer separation on the top of the wing, leading to an unsteady wake structure, with buffet frequencies of around 9Hz – 12Hz, corresponding to a Strouhal number range of St $= 0.10$ – St $= 0.12$, depending on the angle of attack. Buffet frequencies predicted by the CFD matched the flight test frequencies measured by accelerometers to within 2.9% and also matched previous CFD work, which used a similar DES model.

Initial analysis of the DES flow field around key parts of the aircraft structure indicate a significant interaction of the wing wake with the tailplane. Such an interaction would require an investigation of the excitation modes of this structure. To this end, further experimental measurements of the tailplane structure during flight have been made and these will be the subject of a future paper. Further numerical measurements will also focus on extending the DES model, to predict methods to suppress this wake inaction with the tailplane. A significant extension of the DES model with flight path data, would also allow prediction of the incipient spin behavior and the aerodynamics of the full spin. Knowledge of the incipient spin flow field would ultimately allow the aircraft designer to specify aerodynamic sensor positions to warn the pilot of a possible full spin. At the time of writing of this paper, flight path data from a spin is being recorded and analysed for this future work.

References

[1] J. Chambers and H. P. Stough, "Summary of NASA stall/spin research for general aviation configurations.," in *AIAA General Aviation Technology Conference. Anaheim, CA, 29th September-1st October 1986*, Reston: AIAA.

[2] C. Bennett and N. Lawson, "On the development of flight-test equipment in relation to the aircraft spin," *Progress in Aerospace Sciences*, vol. 102, pp. 47 – 59, 2018.

[3] D. V. Rao and T. H. Go, "Optimization of aircraft spin recovery maneuvers," *Aerospace Science and Technology*, vol. 90, pp. 222 – 232, 2019.

[4] M. A. Mcveigb and E. Kisielowski, "A design summary of stall characteristics of straight wing aircraft," Tech. Rep. NASA CR-1646, NASA, 1971. Available at: https://ntrs.nasa.gov/archive/nasa/casi.ntrs.nasa.gov/19710021678.pdf (Accessed: 20 January 2020).

[5] T. Zhou, E. Dowell, and S.-S. Feng, "Computational investigation of wind tunnel wall effects on buffeting flow and lock-in for an airfoil at high angle of attack," *Aerospace Science and Technology*, vol. 95, p. 105492, 2019.

[6] J. Katz and A. Plotkin, *Low-Speed Aerodynamics.* Cambridge Aerospace Series, Cambridge: Cambridge University Press, 2nd ed., 2001.

[7] A. Jameson and K. Ou, "50 years of transonic aircraft design," *Progress in Aerospace Sciences*, vol. 47 (5), pp. 308–318, July 2011.

[8] E. Tinoco, "The changing role of computational fluid dynamics in aircraft development," in *16th AIAA Applied Aerodynamics Conference, Albuquerque,NM,U.S.A., 15 - 18 June 1998*, Reston: AIAA.

[9] L. Zhou, Z. Gao, and Y. Du, "Flow-dependent DDES/ $\lambda - \overline{Re}_{\theta t}$ coupling model for the simulation of separated transitional flow," *Aerospace Science and Technology*, vol. 87, pp. 389 – 403, 2019.

[10] S.-E. Kim, Y. Dai, E. Koutsavdis, S. Sovani, N. Kadam, and K. Ravuri, "A versatile implementation of acoustic analogy based noise prediction method in a general-purpose CFD code," in *9th AIAA/CEAS Aeroacoustics Conference and Exhibit, May 2003*.

[11] F. Mathey, O. Morin, B. Caruelle, and K. Debatim, "Simulation of aeroacoustic sources in aircraft climate control system," in *12th AIAA/CEAS Aeroacoustics Conference (27th AIAA Aeroacoustics Conference), Cambridge, Massachusetts, 8th-10th May 2006*.

[12] R. I. Hoff and G. B. Gratton, "Spin induced aerodynamic flow conditions on full-scale aeroplane wing and horizontal tail surfaces," *The Aeronautical Journal (1968)*, vol. 117, no. 1198, p. 1207–1231, 2013.

[13] N. J. Lawson, N. Salmon, J. E. Gautrey, and R. Bailey, "Comparison of flight test data with a computational fluid dynamics model of a scottish aviation bulldog aircraft," *The Aeronautical Journal (1968)*, vol. 117 (1198), no. 1198, p. 1273–1291, 2013.

[14] D. Raymer, *Aircraft Design: A Conceptual Approach*. Reston, Virginia: AIAA, 3nd ed., 1999.

[15] R. C. J.J. Bertin, *Aerodynamics for Engineers*. Upper Saddle River New Jersey: Pearson, 6th ed., 2013.

[16] in *Springer Handbook of Experimental Fluid Mechanics* (J. F. C. Tropea, A. Yarin, ed.), Berlin Heidelberg: Springer-Verlag, 2007.

[17] J. A. JR., *Fundamentals of Aerodynamics*. New York: McGraw-Hill, 5th ed., 2011.

[18] W. Phillips, *Mechanics of Flight*. New Jersey: Wiley, 2nd ed., 2010.

[19] M. Shur, P. Spalart, M. Strelets, and A. Travin, "Detached-eddy simulation of an airfoil at high angle of attack," in *Engineering Turbulence Modelling and Experiments 4* (W. Rodi and D. Laurence, eds.), pp. 669 – 678, Oxford: Elsevier Science Ltd, 1999.

[20] L. Casadei, L. Könözsy, and N. J. Lawson, "Unsteady detached-eddy simulation (DES) of the jetstream 31 aircraft in one engine inoperative (OEI) condition with propeller modelling," *Aerospace Science and Technology*, vol. 91, pp. 287 – 300, 2019.

[21] C. Bennett, N. Lawson, J. Gautrey, and A. Cooke, "CFD simulation of flow around angle of attack and sideslip angle vanes on a BAe Jetstream 3102 – part 1," *Aerospace Science and Technology*, vol. 68, pp. 561 – 576, 2017.

[22] N. Lawson, H. Jacques, J. Gautrey, A. Cooke, J. Holt, and K. Garry, "Jetstream 31 national flying laboratory: Lift and drag measurement and modelling," *Aerospace Science and Technology*, vol. 60, pp. 84–95, 2017.

[23] C. Bennett, N. Lawson, J. Gautrey, and A. Cooke, "CFD simulation of flow around angle of attack and sideslip angle vanes on a bae jetstream 3102 – part 2," *Aerospace Science and Technology*, vol. 68, pp. 577 – 587, 2017.

[24] P. Spalart, "Young-person's guide to detached eddy simulation grids," Tech. Rep. CR-2001-211032, NASA, 2001. Available at: https://ntrs.nasa.gov/archive/nasa/casi.ntrs.nasa.gov/20010080473.pdf (Accessed: 12 February 2020).

[25] D. Weihs and J. Katz, "Cellular patterns in poststall flow over unswept wings," *AIAA Journal*, vol. 21 (12), pp. 1757–1759, December 1983.

[26] I. Rodríguez, O. Lehmkuhl, R. Borrell, and A. Oliva, "Direct numerical simulation of a NACA 0012 in full stall," *International Journal of Heat and Fluid Flow*, vol. 43, pp. 194 – 203, 2013.